# Documentation of Faults

## Table DR1. Scanned faults and roughness processing

| Name | Scanner | Location | Lithology | Sense | Slip | Processing |
|---|---|---|---|---|---|---|
| Cascia# | LiDAR | 42.719° N 13.002° E | Carbonate | Normal | 50m | Small patches[b] + Taper 5%[d] |
| Gubbio Upper# | LiDAR | 43.344° N 12.597° E | Carbonate | Normal | 50-100m | Small patches[b] + Taper 5%[d] |
| Gubbio Lower# | LiDAR | 43.344° N 12.597° E | Carbonate | Normal | 200m | Small patches[b] + Taper 5%[d] |
| Monte Coscerno# | LiDAR | 42.692° N 12.887° E | Carbonate | Normal | 250m | Small patches[b] + Taper 5%[d] |
| Monte Maggio# | LiDAR | 42.762° N 12.941° E | Carbonate | Normal | 650m | Small patches[b] + Taper 5%[d] |
| Val Casana# | LiDAR | 42.718° N 12.857° E | Carbonate | Normal | 150m | Small patches[b] + Taper 5%[d] |
| Venere Large# | LiDAR | 41.971° N 13.664° E | Carbonate | Normal | >20m | Small patches[b] + Taper 5%[d] |
| Venere Small# | LiDAR | 41.971° N 13.664° E | Carbonate | Normal | 4m | Small patches[b] + Taper 5%[d] |
| West Fucino# | LiDAR | 41.940° N 13.362° E | Carbonate | Normal | ~80m | Small patches[b] + Taper 5%[d] |
| Vasquez rocks# | LiDAR | 34.483° N 118.316° W | Sandstone | Normal | 10±5cm | Small patches[b] + Taper 5%[d] |
| Yeelim# | LiDAR | 31.223° N 35.354° E | Carbonate | Normal | 50-80m | Small patches[b] + Taper 5%[d] |
| Split Mountain# | LiDAR | 33.014° N 116.112° W | Sandstone | Strike-slip | 30±15cm | Small patches[b] + Taper 5%[d] |
| Mecca Hills# | LiDAR | 33.605° N 115.918° W | Carbonate | Strike-slip | 20±10cm | Small patches[b] + Taper 5%[d] |
| Flowers Pit# | LiDAR | 42.077° N 121.856° W | Andesite | Normal | 100-300m | Small patches[b] + Taper 5%[d] |
| Chimney Rock# | LiDAR | 39.227° N 110.514° W | Carbonate | Normal | 8m | Small patches[b] + Taper 5%[d] |
| Lake Mead# | LiDAR | 36.062° N 114.831° W | Dacite | Normal | 500-1000m | Small patches[b] + Taper 5%[d] |
| Corona Heights* | LiDAR + LP[a] | 37.765° N 122.437° E | Chert | Strike-slip | Several m to >1km | Small patches[b] + Large patches[c] + Taper 3%[d] |
| Vuache-Sillingy* | LiDAR + LP[a] | 45.920° N 6.049° E | Carbonate | Strike-slip | 10-30m | Small patches[b] + Taper 3%[d] |
| Dixie Valley* | LiDAR + LP[a] | 39.947° N 117.945° E | Rhyolites | Normal | Several m to >3-6km | Small patches[b] + Taper 3%[d] |
| Bolu* | LiDAR | 40.685° N 31.568° E | Carbonate | Strike-slip | 20m-85km | Small patches[b] + Taper 3%[d] |
| Klamath## | LiDAR | 42.135° N 121.678° W | Basalt +andesite | Normal | 50-300m | Large patches[c] + Taper 3%[d] |

| | | | | | | |
|---|---|---|---|---|---|---|
| Arkitsa§ | LiDAR | 38.733° N<br>23.000° E | Carbonate | Normal | >300-400m | Large patches[c] + Taper 3%[d] |

Sources: # Brodsky et al. (2011), *Candela et al. (2012), ## Sagy et al. (2007), § Resor and Meer (2009)
Notes: [a] Laser Profilometer, [b] Small clean fault patches free of unwanted objects are selected from the original cloud of points, [c] Large clean fault patches are obtained by removing locally non-faulting features from the original cloud of points, [d] During the processing of individual profiles for computing the Fourier spectra we either apply a cosine taper of 3% or 5%.

## Scale-dependent roughness in spatial maps

Figure DR1 demonstrates that the scale-dependent roughness is a feature of individual profiles of the raw data in the spatial domain. The parameterization in the Fourier domain usefully captures the same phenomenon shown in Figure DR1.

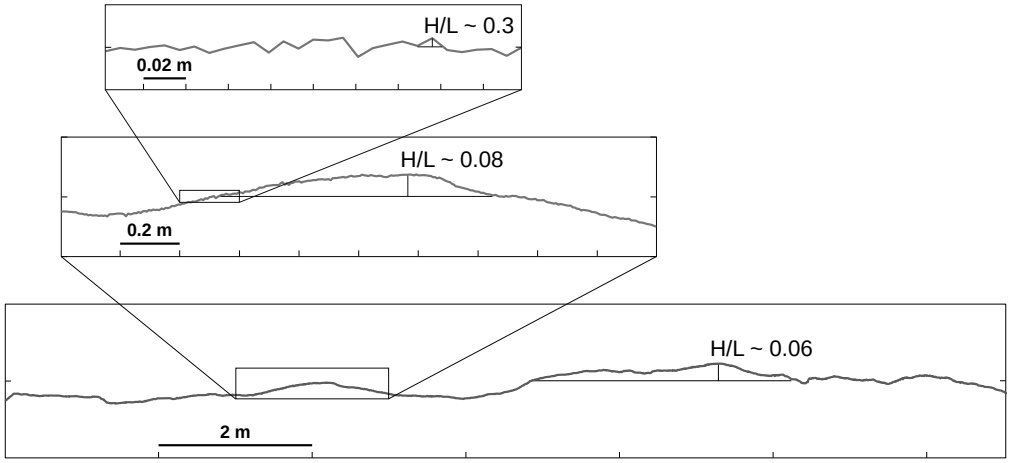


**Figure DR1. Example cross sectional profiles at different magnifications showing the scale dependence of the aspect ratio, *H/L*.** Profiles are taken from a ground-based LiDAR scan of the Corona Heights fault surface. Panels show sections through the fault at different magnifications (Note the scale bar is different in each panel).

## Fourier Transform Computation

From each fault patch (LiDAR or profilometer), hundreds to thousands of profiles are extracted in the slip direction. Most fault patches have more than 500 profiles in the slip direction and all patches have at least 100. The four steps in the procedure to compute the spectrum of each profile are as follows: (1) Each profile is detrended by subtracting the best-fit trend. (2) Either a 3% or 5% cosine taper is applied to each rough profile to ensure that there are no step functions at the end of the finite window. (3) The discrete Fourier transform is calculated, and the power spectrum is equal to the square of the amplitudes of the coefficients. (4) The power spectrum is normalized by the profile length to obtain the power spectral density. The mean Fourier spectrum of each fault patch is then computed by averaging the spectra of the profiles and restricting the results to well-resolved wavelengths that are more than a factor of 2 less than the profile length. Finally we smooth the spectra in frequency space by binning each averaged spectrum into 20 logarithmically-spaced intervals in the well-resolved frequency space and averaging the power spectral density within the bin. Logarithmic binning provides a constant density of data points in the logarithmic representation and therefore avoids giving more weight to smaller scales in subsequent fitting procedures.

## Maximum Shear Strain in Hertzian Contacts

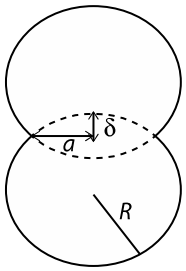


**Figure DR2.** Cartoon of elastic interaction between two spheres. Dashed lines show undeformed outlines.

The elastic deformation between two identical spheres was first modeled by Hertz (Hertz, 1881). We use the solution to illustrate the general form of the elastic stress field between contacting asperities starting from the general results summarized by Johnson, 1985, Appendix 3. If two elastic spheres of radius $R$ are in contact as shown in Figure DR2 and the contact between them has no shear stress, the solution for the radius $a$ of the contact area is

$$a = (3WR/4E')^{1/3} \qquad \text{(A1)}$$

where $W$ is the loading force on the sphere and $E'$ is the modified Young's modulus $(2(1-\nu^2)/E)^{-1}$ and $E$ is the Young's modulus and $\nu$ is the Poisson ratio. The approach distance between the two spheres is related to the contact radius by

$$\delta = a^2/R \qquad \text{(A2)}$$

Slightly manipulating eq. A1 yields

$$a/R = \tfrac{3}{4}\,\pi\, W/(E'\pi a^2) \qquad \text{(A3)}$$

Since $W/\pi a^2$ is by definition average normal stress $\sigma$ on the contact, then combining eq. (A2) and (A3) yields.

$$\delta/a = \tfrac{3}{4}\,\pi\,\sigma/E'. \qquad \text{(A4)}$$

Complete solutions show that the maximum shear stress $\tau$ within the asperity is 0.31 the maximum normal stress, and the maximum normal stress is $3/2\ \sigma$ (Johnson, 1985, Appendix 3). For complete flattening of a contact of height $H$ and length $L$, $\delta=H$ and $a=L/2$. The shear stress is related to the shear strain by $\tau=2G\varepsilon$ where $G$ is the shear modulus. Therefore,

$$H/L = \pi/0.62\quad \varepsilon\, G/E' \qquad \text{(A5)}$$

and the shear strain is proportional to the aspect ratio as expected. The maximum shear strain occurs in the interior of the asperity and therefore the asperity fails rather than the contact surface. Including friction at the interface does significantly affect the internal stress field of the contacting spheres (Johnson, 1985; Sect. 5.4).

Similar solutions are recovered for more complex geometries. For a sinusoidal, single-wavelength surface, the normal stress required for complete flattening of the asperity is $2^{1/2}\,\pi\,E'\,H/L$, which implies a similar scaling with strain as in (A5) (Johnson et al., 1985). Multi-scale models also preserve the proportionality between calculated stresses, strains and aspect ratio (Krithivasan and Jackson, 2007; Jackson et al., 2012).

The role of surface slope in determining surface failure during shearing has long been recognized in tribology. For instance, the plastic yield criteria for an indentor depends on the cotangent of the apex angle, which is the aspect ratio $H/L$ (Johnson et al., 1985; Sect. 6.1). As a result, wear mechanisms are predicted by using the plasticity index $\psi \equiv (H/L)E'/\mathcal{H}$ where $\mathcal{H}$ is the hardness (Mikic, 1974; Johnson, 1985). The related approach presented here focuses on the inverse problem of determining strength of a material given the observed surface roughness.

**References**


Hertz, H., 1881, On the elastic contact of solids. J. Reine Angew. Math 92, 156–171.

Jackson, R.L., Ghaednia, H., Elkady, Y.A., Bhavnani, S.H., and Knight, R.W., 2012, A closed-form multiscale thermal contact resistance model: IEEE Transactions on Components, Packaging and Manufacturing Technology, v. 2, no. 7, p. 1158–1171, doi: 10.1109/TCPMT.2012.2193584.

Johnson, K.L., 1985, Contact Mechanics: Cambridge University Press, Cambridge.

Johnson, K.L., Greenwood, J.A., and Higginson, J.G., 1985, The contact of elastic regular wavy surfaces: International Journal of Mechanical Sciences, v. 27, no. 6, p. 383–396, doi: 10.1016/0020-7403(85)90029-3.

Krithivasan, V., and Jackson, R.L., 2007, An analysis of three-dimensional elasto-plastic sinusoidal contact: Tribology Letters, v. 27, no. 1, p. 31–43, doi: 10.1007/s11249-007-9200-6.